Dry sliding wear investigation on tungsten carbide particles reinforced iron matrix composites

A Grairia[1,4] , N E Beliardouh[2,4], M Zahzouh[1], C Nouveau[3] and A Besnard[3]

[1] Metallurgy and Materials Engineering Laboratory (LMGM), University Badji Mokhtar of Annaba BP 12, Annaba 23000, Algeria
[2] Surface Engineering Laboratory (L.I.S), University Badji Mokhtar of Annaba BP 12, Annaba 23000, Algeria
[3] Laboratoire Bourguignon des Matériaux et Procédés (LaBoMaP), Arts et Métiers ParisTech de Cluny, Rue Porte de Paris, F-71250, Cluny, France
[4] Authors to whom any correspondence should be addressed.

E-mail: amina.grairia@univ-annaba.org and beliardouh_23@yahoo.fr

Abstract

WC particles reinforced Fe-based metal matrix composites were synthesized by powder metallurgy process. The microstructure and composition of the specimens were analyzed and the wear-resistant properties against WC and alumina balls were comparatively investigated by SEM/EDS analyses. The wear rates of specimens were evaluated by optical profilometry. Microstructure exhibited austenite Fe-FCC dendrites, eutectic (iron austenite + carbides) and primary carbides. Two wear mechanisms have been identified from SEM as main mechanisms during dry sliding wear of Tungsten carbides reinforced iron matrix, namely oxidation and abrasion. The overall wear performance, which is obtained by considering the wear loss of the substrates, indicated less resistance against Alumina compared to WC ball contact.

1. Introduction

Particles reinforced metal matrix composites (MMCs) are a large kind of composite materials, consisting of at least, two-phase microstructures of hard particles (reinforcement) embedded uniformly in a metallic matrix (binder) such as W, Co, Ni, Fe, Al or a combination of them (two or more elements i.e. Al–Mg, W–Co, Fe–Ni). The particles of reinforcements are ceramic, metallic or organic compounds. Nowadays MMCs are of a great interest due to their enhanced mechanical properties such as a specific strength [1].

To fabricate particles reinforced metal matrix composites, various processing ways such as powder metallurgy, conventional casting, self-propagating high-temperature synthesis [2–5], selective laser melting [6] etc, have already been developed. Among these manufacturing processes, powder metallurgy processes allow adjustment of the composition, fraction and distribution of the reinforcements. The deal is to obtain net shape parts with complex geometries at a reduced cost via a total elimination of additive manufacturing operations [7].

In particle reinforced iron matrix composites (PRIMCs), the particle reinforcements often used are carbides, nitrides, oxides because of their good physical and chemical properties [8–10]. Other particles are also reported in the literature such as zirconia toughened alumina (ZTA) [11]. By combining physical and mechanical properties, which is not achievable with classical ferrous materials (steels and cast iron), the PRIMCs offer many opportunities for developing new materials. Ceramic carbide reinforced iron matrix composites have been demonstrated to be low-cost and easy controlled technologies [12–14]. The carbides are mainly formed by strong carbide formers, i.e. Ti, V, W, Mo, Nb, Cr etc. During powder metallurgy process, various types of carbides, such as M_6C, M_2C, MC and $M_{23}C_6$, can be formed, depending on the alloy composition and processing parameters such as sintering temperature and cooling rate. Controlling the amount of carbon in the system and a good bonding at the carbide/matrix interfaces are the main factors influencing final mechanical properties of carbide reinforced iron matrix composites [15, 16].

By creating more thermodynamically stable carbide reinforcements based on their nucleation and growth from the parent matrix phase, it was possible to avoid the interface incompatibility; the carbides can grow directly from the melt during solidification or they are created by eutectic reaction or by decomposition of other types of carbide. This technique, called *in situ* synthesis, was developed extensively and has been applied to synthesize iron matrix composites such as Fe–TiC, Fe–VC, Fe–SiC, Fe–TaC, etc and their hybrid mixture [5, 6, 8, 16–19]. Among them, Tungsten carbide (WC) takes a leading position in industrial applications. It is one of the most suitable reinforcements for the iron matrices because of its availability, high hardness ($HV_{0.1} \sim 2280$), high melting point, and finally good thermodynamic stability [20, 21].

It can be used for *in situ* synthesis of carbide-reinforced iron matrix composites with high macro-hardness and toughness and for the manufacturing composites, machining tools, and many wear-resistant components [15, 22].

The WC consolidation processing of MMCs is generally performed through liquid-phase sintering above the eutectic temperature, owing to the high melting point of tungsten ($\sim$3420 °C). However, the addition of brittle ceramic WC particles may degrade toughness as the reinforcing particles promote crack initiation as reported by previous studies [15, 22, 23]. Besides, the final mechanical properties of the composite materials depend on their manufacturing route, relative density and the volume fraction of WC particle reinforcements [20, 24].

Considering wear resistance, the effects of microstructural components i.e. size and volume fraction of both WC particles and pores, are not so straightforward. Resistance against erosion wear of the Fe-WC surface composites was studied by Zhou *et al* [20]. Their results indicate that (i) the wear rates strongly depend on volume fractions of WC reinforcing particles; (ii) there is no linear relation between % volume of WC particles and wear rates. Moreover, Li *et al* [25], reveal the positive role of Cr content in the matrices on the three-body abrasive wear resistance of the Fe-WC composites.

It is noteworthy that the porosity has been reported in some studies as beneficial and in others as detrimental. For example, Sinha *et al* [26] reported that wear rate increased with the porosity content due to synergic effect of real contact area and subsurface cracking. However, porosity may help to absorb impact energy that accompanies crack splitting, which reduces crack propagation as revealed by Chen [27]. Authors agree that a trade-off exists between wear resistance and toughness of the conventional MMCs materials. The toughness is usually improved at the expense of the wear resistance and vice versa.

In this study, an attempt is made in the development of a new material through powder metallurgy technique by the addition of small proportion of Ni which stabilizes the iron matrix structure. The microstructure was investigated and the tribological performances are determined and discussed in details.

2. Material and methods

2.1. Material preparation
WC particles reinforced iron matrix composite specimen, indicated by FNW (Fe–Ni–W), was elaborated from precursor obtained by chemical reduction methods. Fe was formed from Fe_2O_3 and Ni powder was made from nickel acetate [$Ni(CH_3COO)_2$–$4H_2O$]. A WC commercially powder carbides was added as a reinforcing agent. All elemental powders are less than 45 μm in size.

Conventional powder metallurgy route was used. It involves mixing the metal powders by ball milling for 24 h at a ball-to-mixture ratio of 3:1 and 100 rpm of rotation speed according to the designed composition of 85Fe–5Ni–10WC. Then, the prepared powders were blended with 5 wt% paraffin wax and cold compacted at pressure of 200 bars. Finally, the compacted powders with dimensions 20 mm $\times$ 20 mm $\times$ 10 mm were obtained.

Then, specimens were pre-sintered at 800 °C for 1 h. Afterwards a liquid-phase sintering at 1520 °C for 2 h was conducted. All thermo-treatments were conducted under hydrogen protective atmosphere. The temperature-time parameters of sintering were adopted as a result of many experiments. Table 1 indicates the influence of sintering temperature on physical (density, porosity) and mechanical properties (hardness) of the synthesized samples. So, that is the reason for choosing 1520 °C i.e. the optimum properties (low porosity and high density/hardness).

2.2. Tribological test
Prior to any experiment, the samples were carefully polished with successive SiC papers and finished by diamond paste (0.25 μm), rinsed, ultrasonically cleaned in acetone and finally dried in pressurized air. Tribological tests were conducted with a pin-on-disc tribometer (*CSM HT1000*) and the Tribox 4.1.1 software, using a ball on disc configuration in which the specimen acts as the disc that turns in contact with a static partner (alumina or WC ball) under dry-sliding conditions. During the tests, two sliding speeds ($v = 5$ cm s^{-1} and 10 cm s^{-1}), and two normal loads (F $= 5$ N and 10 N) were combined. The sliding distance (200 m) and track

Table 1. Influence of sintering temperature on physical and mechanical properties of the synthesized samples.

Sintering temperature (°C)	Relative density (g/cm³)	Hardness (HRc) average value	Porosity (%)
1100	7.32	7.5	24
1200	7.52	23.7	18
1300	7.56	36	15
1400	7.76	42	12
1520	8.23	58	2

radius (r = 4 mm) were kept constant. The tests were conducted at room temperature (20 °C–25 °C) and (40–45)% humidity. In order to compare the wear resistance of the specimens, specific wear rates were calculated according to equation (1):

$$\mathbf{K} = \frac{\boldsymbol{V}}{\boldsymbol{L.F}}$$

(1)

Where K is the specific wear rate [mm³/N m], V is the wear volume [mm³], F is the normal load [N] and L is the sliding distance [m]. The ball counterparts were:

- Al_2O_3 High purity (99.5%) α-Alumina (hardness H = 16.14 GPa; arithmetic average (R_a) and the quadratic mean (Rq) surface roughness were 178 and 256 nm, respectively).

- WC Cemented tungsten carbide, 6% Co (H = 15 GPa; R_a = 125 and Rq = 173 nm), supplied by *CSM Instruments.*

An optical profilometer *(VEECO-Wyko NT1100)* was used to measure the wear volume loss. Two wear tests were performed per sample i.e. each sample was tested at least twice to ensure repeatability of the results. In order to analyze the wear process and consequently the wear mechanisms, the worn surfaces and wear debris generated during these tests were observed by SEM *(Jeol 5900LV)* and analyzed by EDS/WDS.

3. Results and discussion

3.1. Microstructure

Since the hard metal compacts are predominantly densified by liquid phase sintering, the sintering temperature of 1520 °C was selected to have at least one phase of the systems in the liquid state, and lies above the eutectic temperature. The knowledge of the phase equilibrium diagram of (Fe–Ni)–WC is generally used to predict the phases after the sintering step. The Fe–Ni–WC systems show eutectic compositions richer in the carbide component [28]. Besides, in the investigated specimen of the current work, solid solution matrix is the main phase. The last transformation during solidification is eutectic, so the microstructure must contain at least three phases namely the matrix (iron solid solution), primary carbides and the eutectic phase.

Phase identification, using XRD analysis, was accomplished by comparing the peaks and relative intensities from the investigated specimen with those taken from current standard files. Figure 1 shows the obtained XRD patterns (Cu-Kα radiation). It consists of iron austenite (γ-Fe), M_6C (most probably Fe_3W_3C carbides), W_2C carbides and primary WC carbides corresponding to JCPDS Files No.: 31-0619, 41-1351, 02-1134, and 25-1047, respectively.
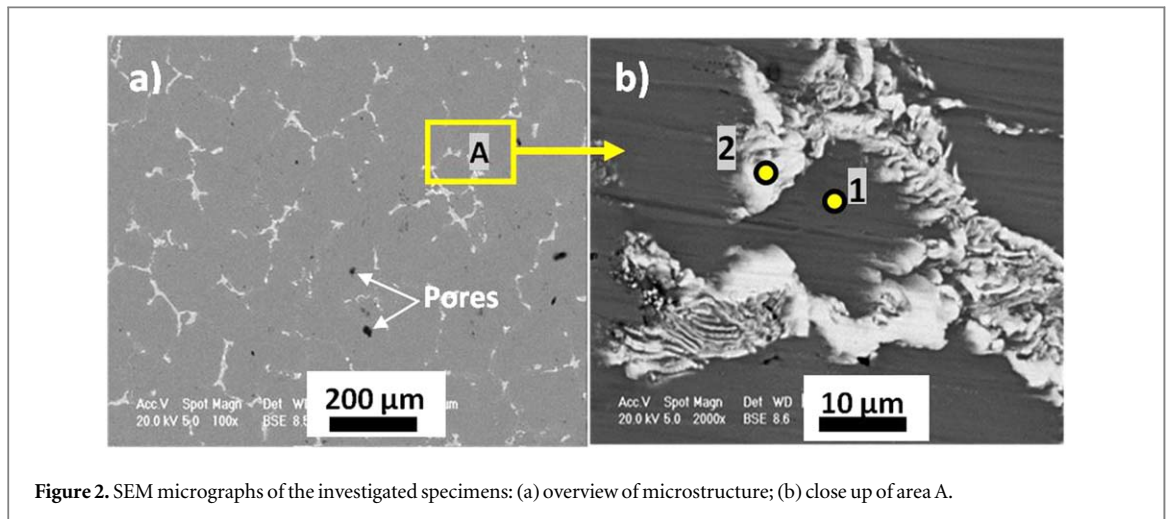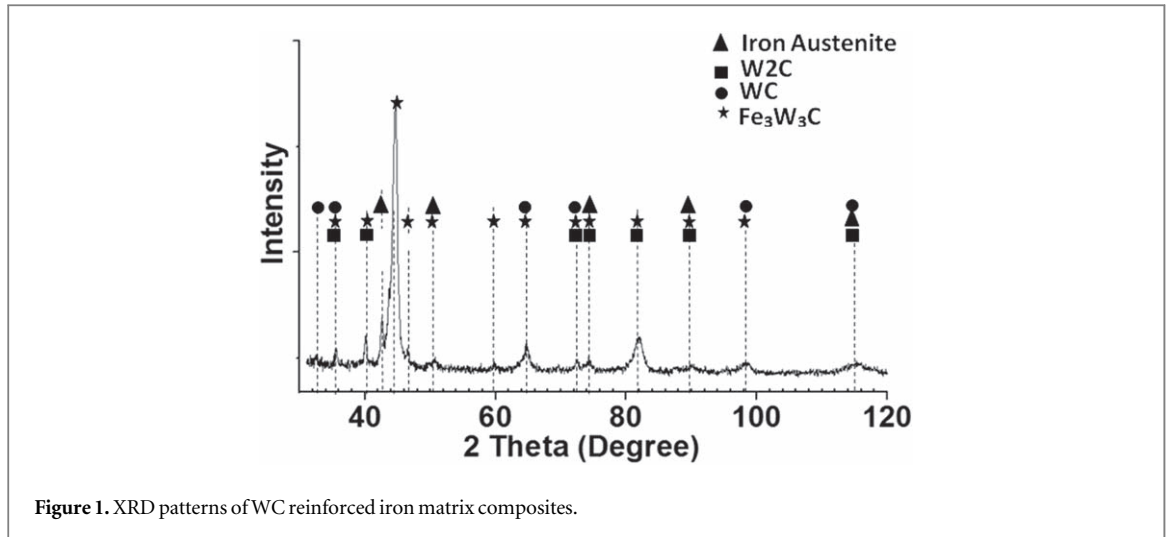
SEM micrographs of investigated specimens are shown in figures 2(a)–(b). As a result, the microstructure consists of solid solution i.e. iron austenite γ-Fe, (figure 2(b); label '1') composed of 79.5%Fe, 3.7%Ni, 13.4%W and % C balance (in weight %), surrounded by a more-or-less connected network of large primary carbides (figure 2(b); label '2') with a nominal composition of 68.6%Fe, 2.4% Ni, 24.7%W and %C balance (in weight %), and eutectic [austenite (γ-Fe) + (W, Fe, Ni) C].

This microstructure was known as 'fish-bone' eutectic form or 'Chinese script morphology' [25].

Besides, there are a few superficial and internal pores obviously existing in the tested specimens after 1520 °C sintering as shown in figure 2. The LPS temperature and the content of (Fe + Ni) are of crucial importance to eliminate the pores and to prevent the excessive grain growth [29].

3.2. Friction coefficients evolution

The dependency of friction coefficient was evaluated on the number of cycles with a standard number of 8000. During the ball-on-disc tests, friction coefficients were continuously recorded for the couples: FNW tested specimens against WC–Co and alumina balls as counterparts.

Figure 1. XRD patterns of WC reinforced iron matrix composites.

Figure 2. SEM micrographs of the investigated specimens: (a) overview of microstructure; (b) close up of area A.

3.2.1. FNW versus WC balls

Against WC balls as counterfaces, the COF of all tribological couples in contact increases abruptly during the first cycles of sliding. Then it subsequently goes through an intermediate stage and gradually tends to a steady-state (figures 3(a)–(b)). In the intermediate stage, the COF of the tested specimens at 10 N, decreased to a minimum value of 0.35 and 0.5 for 5 cm s^{-1} and 10 cm s^{-1}, respectively. The drop in the COF could be associated with a drop-in plowing component of friction as a consequence of smoothing of both hard surfaces in contact. Then, the COF increases again because of generation and entrapment of wear particles. This phenomenon was described in detail by many authors [30, 31]. In the next step, the COF increases to a steady state as the sliding progresses. The situation observed at 5 N was not so different; the intermediate stage was very short in the case of 10 cm s^{-1}, approximately 1000 cycles while it reached 4000 cycles in the other cases. The COF values at steady-state are listed in table 2.

3.2.2. FNW versus Alumina balls

When sliding against alumina balls, the COF evolution of the tested specimens at 5 N and 10 N exhibited different curve tendency (figures 3(c)–(d)). During the initial stage at 5 N of applied load (figure 3(c)), the COF reached a high value (around 1.0 ± 0.15). Here, the asperities were fractured and the coefficient of friction increases as the number of wear particles rapidly increase. Then, in the intermediate period, a drop in friction to a relatively lower value (1.0) was observed for a sliding of ~1000 cycles. This period was not so obvious at 10 cm s^{-1} and could be due to the amount of ejected debris [30]. The COF slowly increases to a steady state stage. It took around 2000 cycles for the COF to reach its steady state value of 0.97 and 1.09 at 10 and 5 cm s^{-1} of sliding speed, respectively.

At 10 N of applied load (figure 3(d)), the tribological couples had a high run-in friction. The COF increases immediately at the beginning of the test until a maximum value of 0.93 ± 0.01. Next, it decreases to the steady
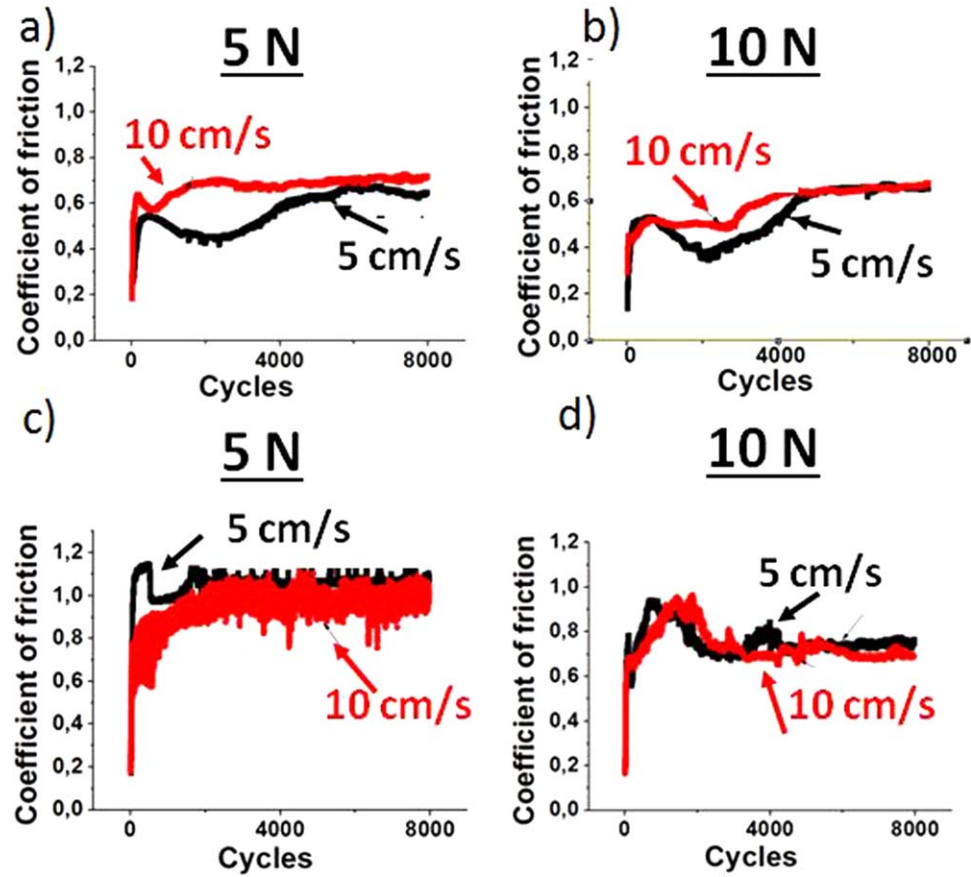
Figure 3. Friction coefficient evolution of FNW samples against: (a)–(b) a WC and (c)–(d) an alumina ball.

Table 2. Values of coefficient of friction (COF) at constant periods and average surface roughness of wear tracks.

Samples Test parameters (Load/Sliding speed)	WC balls			Alumina balls		
		Surface roughness (μm)			Surface roughness (μm)	
	COF	Ra	Rq	COF	Ra	Rq
5 N/5 cm.s^{-1}	0.64 ± 0.02	6.05	3.86	1.15 ± 0.02	2.36	3.05
5 N/10 cm.s^{-1}	0.7 ± 0.01	6.17	3.07	0.98 ± 0.01	1.17	1.48
10 N/5 cm.s^{-1}	0.65 ± 0.01	4.26	2.49	0.74 ± 0.02	1.01	1.40
10 N/10 cm.s^{-1}	0.65 ± 0.01	5.01	2.59	0.7 ± 0.02	1.48	1.96

state period. The drop in friction is maybe a consequence of particles ejection formed in the run-in stage [30]. At the steady state period, the COF values are listed in table 2. Finally, the average value of the COF, at steady state, depends on the applied load regardless of sliding speed. The highest COF are found in FNW/Alumina ball contacts.

The roughness parameters (Ra, Rq) of the worn surfaces of the FNW samples are also listed in table 2. It is well established that initial surface roughness has a considerable influence on finale properties of wear [32]. In this work, the influence of surface roughness parameters, on COFs and wear rates (statistical studies) was not considered. From table 2, it can be seen only, that WC ball produces higher surface roughness parameters than alumina ball. It is therefore difficult to draw general conclusions from the obtained results.

3.3. Wear mechanism

3.3.1. WC balls

Figure 4 shows SEM morphology of the worn surfaces of specimens after 200 m of sliding distance at conditions mentioned above ([5 N;10 N] and [5 cm s^{-1}; 10 cm s^{-1}]). These surface states correspond to the steady-state stage of wear. It occurs when sufficient amount of wear product has been removed involving removal of the
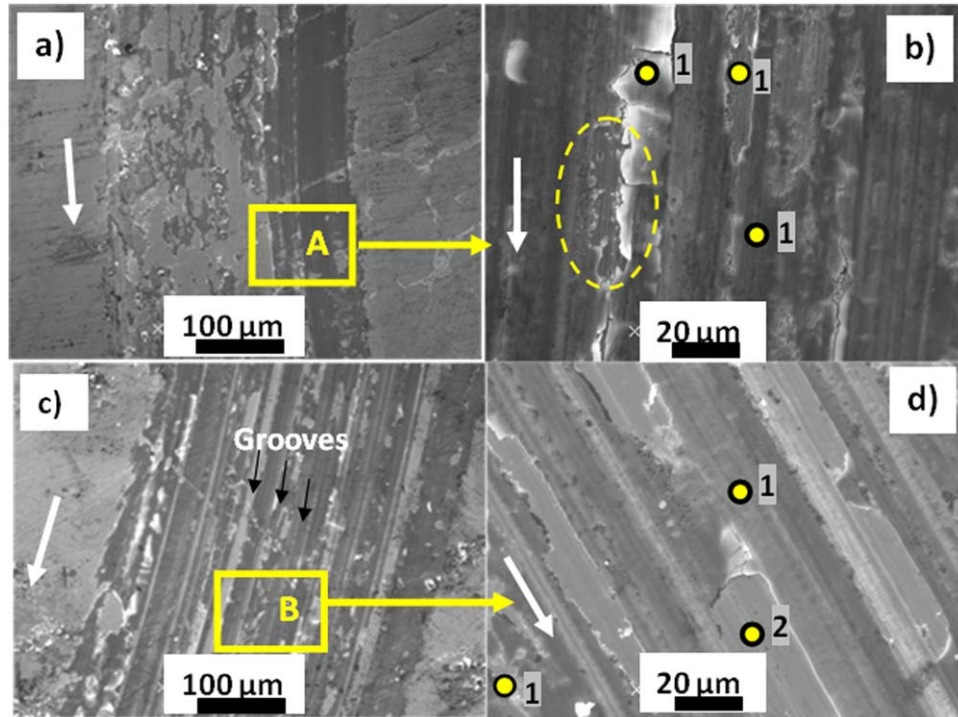
Figure 4. SEM micrographs of wear track of FWN samples against WC balls (a) 5 N/5 cm s^{-1}; (b) close-up of zone A; (c) 5 N/10 cm s^{-1}; (d) close-up of zone B; Sliding directions are indicated by white arrows, label 1: oxidized area and label 2: zone free of oxygen.

carbide grains from the surface. Figures 4(a)–(d) show the wear tracks of specimens at 5 N (5 cm s^{-1} and 10 cm s^{-1}). There are no marked differences between the low and high speed. Wear debris formation and deep grooves parallel to sliding direction can be observed. Such features are characteristics of abrasion, in which hard asperities (two body wear) of the counter face or hard particles (three body wear) plough through the FNW specimens. Abrasion plays a significant role in the wear process as depicted by grooves along the wear track. Besides, EDS analysis of worn surfaces reveals the presence of FNW specimen elements, ball elements and oxygen i.e. Fe, W, Ni, C and O, indicated by label '1' in figures 4(b) and (d). Therefore, it was found that tribo-oxidation took place in the initial sliding contact followed by a severe abrasive wear i.e. the wear particles generated were entrapped subsequently in the sliding contact, causing oxidative wear and three-body abrasive wear of the surfaces. Some residual areas (indicated by label '2') are free of oxides (no oxygen) inside the wear track.

No Cobalt (Co) was detected by EDS analysis, thus the presence of the Tungsten (W) is not a proof that transfer from the WC ball to the disc occurred. Inside the wear track, friction causes local rises of temperature between surfaces in contact; as a result, a mechanically mixed layer or tribo-layer formation appears adhesively attached to the worn surface. The tribo-layer was made of wear debris from antagonist partners and oxygen (oxidation). After more and more cycles of sliding, the tribo-layer becomes brittle. Next, the tribo-layer transforms to wear debris as described by Findik [33].

Figure 4(b) also shows SEM micrograph of wear track revealing breaking of tribo-layer into 'Microchips' of wear debris agglomerated (elliptical zone in yellow). Figures 4(c)–(d) show the wear scar of tested specimen at [5 N; 10 cm s^{-1}]. The increase of the sliding speed does not affect the wear mechanisms. In some areas of the wear scar, 'flakes' of wear debris were completely removed from the inter-groove areas as clearly shown in figure 4(d). The same features are found on worn surfaces at 5 cm s^{-1} (or 10 cm s^{-1}) of sliding speed under 10 N, as can be seen in figures 5(a)–(b) i.e. deep and parallel grooves with the presence of oxygen (EDS spectrum 1) inside the wear track in areas indicated by '1'. Areas free of oxides (EDS spectrum 2) are indicated by label '2'.

The formation of grooves is as follows: the load applied between the ball and the disc can be divided into two components: a normal and a shear stress as reported in the literature [17]: the normal stress allows the abrasive particles (hard oxides, carbides) penetrate the surfaces of FNW composite while the shear stress allows the abrasive particles plough the surfaces of samples parallel to the sliding direction. As a result, the abrasive particles eventually remove or push the materials into 'ridges' along the grooves (figures 5(a)–(b)). Therefore, in the dry sliding wear of FNW/WC balls pair, the oxidative wear was observed as one of the common features at both
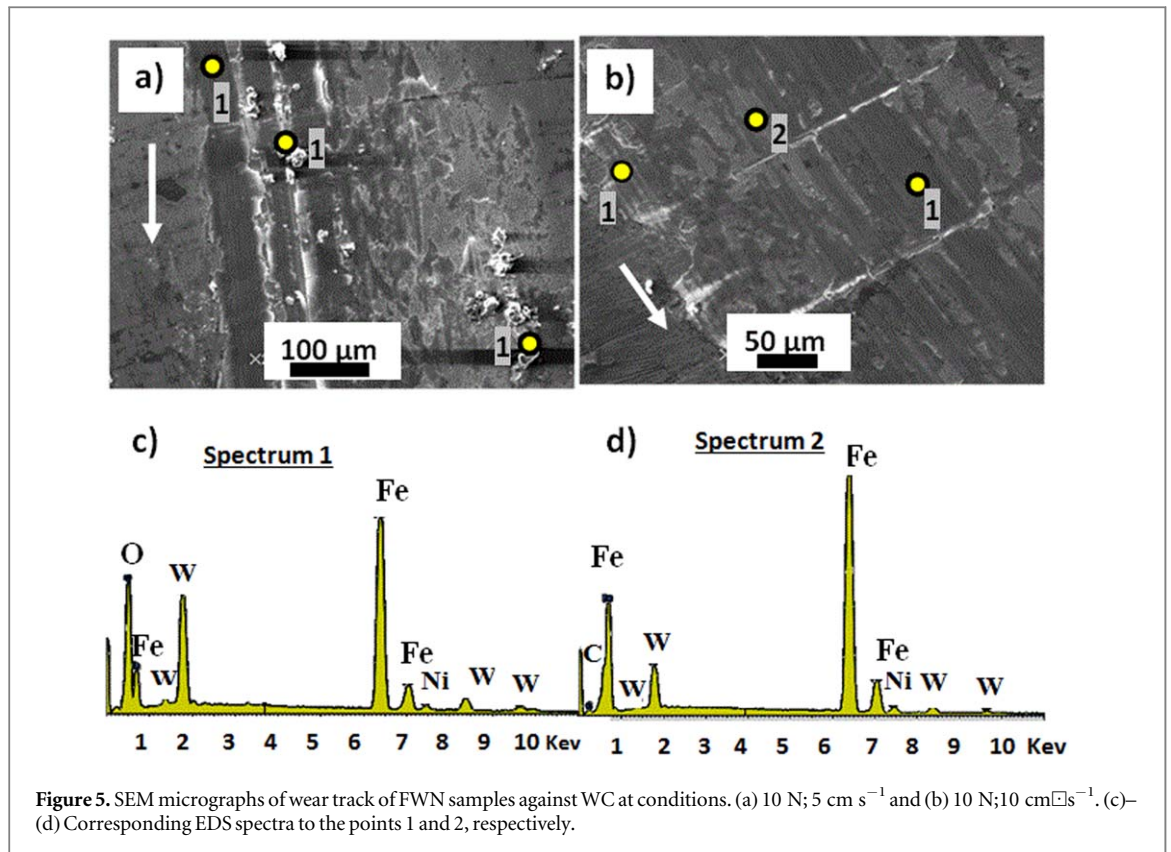
Figure 5. SEM micrographs of wear track of FWN samples against WC at conditions. (a) 10 N; 5 cm s^{-1} and (b) 10 N;10 cm□s^{-1}. (c)–(d) Corresponding EDS spectra to the points 1 and 2, respectively.

lower and higher loads. In fact, these two systems (5 N and 10 N) undergo the same mechanism of wear but at 10 N, the tested surfaces are more damaged.

Finally, two processes took place: oxidative and abrasive wear. The sliding speed parameter had apparently no real influence on the wear mechanism of the FNW/WC ball pairs.

3.3.2. Alumina balls

The SEM morphology of the worn surface of FNW specimen at [5 N and 5 cm s^{-1}] is shown in figures 6(a)–(b). Grooves and wear debris are observed. The EDS analysis was carried out in many areas of the worn surface, at least six per specimen. The occurrence of Fe, W, Ni, C and O peaks, in the EDS spectra (label '1', in figure 6(b)) indicates the existence of carbides and oxides within the analyzed area. These elements are also detected on the agglomerated wear particles. So, the main wear mechanisms seem to be oxidative and abrasive wear. Figure 6(c) shows an overall view morphology of the worn surface at [5 N; 10 cm s^{-1}]. It reveals grooves and many white particles on worn surfaces (wear debris). These wear debris are oxides and carbides.

During abrasion, material removal from the surface occurs by ploughing. The material was displaced to the grooves edges and as a result the formation of 'ridges' occurred as shown in figure 6(c). At 10 cm s^{-1} of sliding speed, the formation of oxidized areas over the worn surface was easier thanks to the increase of the frictional heat. No zone was free of oxygen as presented by labels '1' in figures 6(c)–(d).

A higher magnification SEM micrograph shows flaws caused by individual particles, probably primary carbide, removed from the matrix. Subsequently, the voids were filled with wear products. An example was presented (circled) in figure 6(d). In addition, some very small cracks could be detected on the worn surface. These cracks are provoked by the fatigue of the material and mostly propagated along the eutectic phases as reported by previous studies [31, 34, 35]. These authors explained that cyclical load could cause fatigue cracks on the interphase or intergrain boundaries after series of cycles. Pores in the subsurface can act as local stress concentrators and then origin of cracks [36]. EDS analysis also confirmed that oxygen concentration was rich on the worn surface and that there is no area free of oxides within the wear tracks. Thus, the increase in speed results in a total oxidation of the wear track. The wear mechanism seems to be basically oxidative and abrasive.

Figures 7(a)–(b) illustrate the worn surface of tested specimen at [10 N and 5 cm s^{-1}]. The SEM micrographs revealed the formation of grooves and 'ridges' parallel to the sliding direction. Besides, some of the eutectic features are still visible as clearly shown in figure 7(b). The wear particles released from the surface are crushed and milled into fine fragments. Removal of hard phase fragments from the matrix, leave voids and holes. A detail
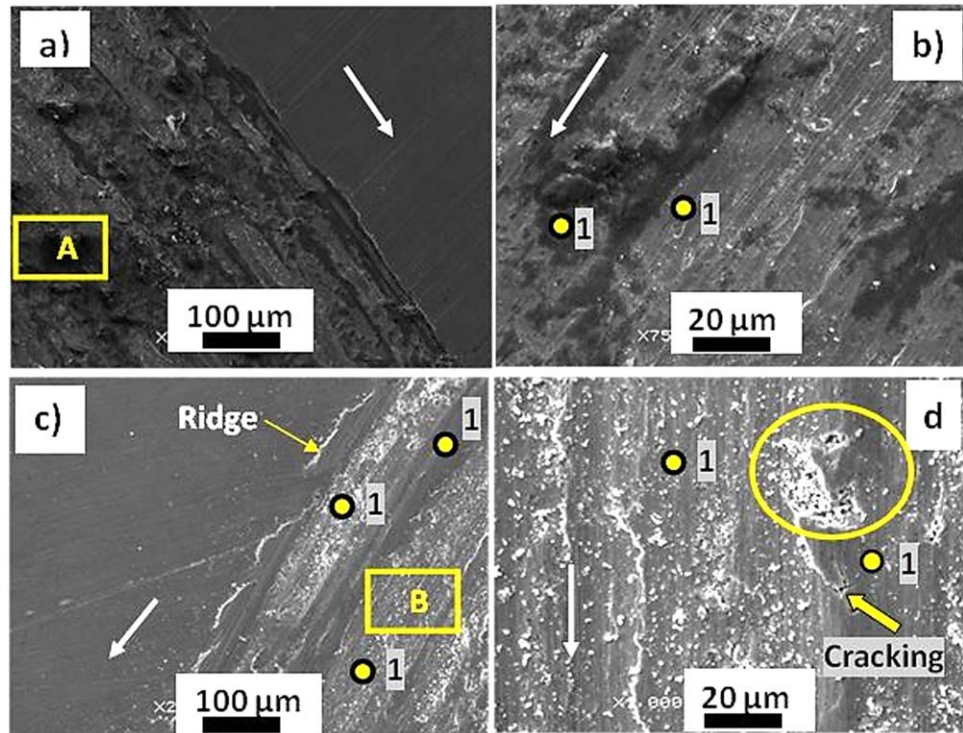
Figure 6. FWN samples against alumina balls at 5 N (a)–(b) 5 cm s^{-1} of sliding speed, (c)–(d) 10 cm s^{-1} of sliding speed. Elliptical area shows the flaw of a particle, which was removed.
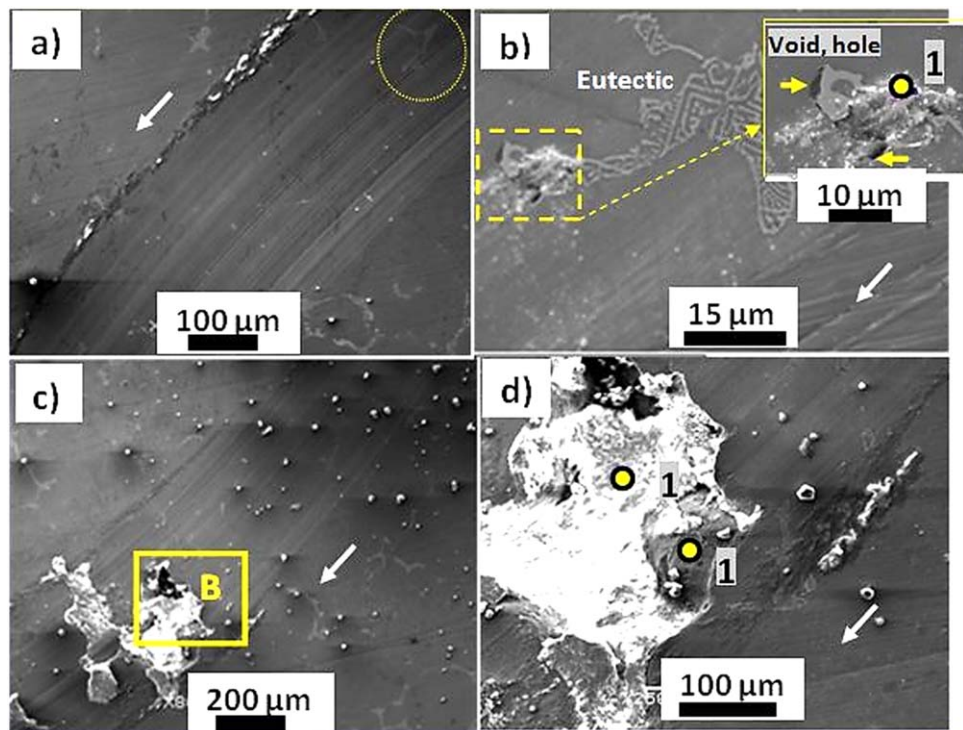

Figure 7. FNW specimen against alumina ball at 10 N and 5 cm.s^{-1}. (a) Overview of the wear track. (b) Details of fishbone-like eutectics formed inside the wear track. (c) FNW versus alumina ball at 10 N and 10 cm s^{-1} conditions. (d) Close up of zone 'B'.

Table 3. The global qualitative results of the SEM/EDS analysis performed on the worn surfaces after tribo-tests.

	Wear track			
Tribo-pair	Zone 1	Zone 2	wear debris (ridge, isolated particles)	
Load = 5 and 10 N Speed = 5 and 10 cm s^{-1}	Oxidized areas Two (02) types of EDS spectra	Areas free of oxides	Three (03) types of EDS spectra	SEM images
FNW/WC Ball	–Fe, W, Ni, C, O	–Fe, W, Ni, C	–Fe, W, Ni, C, O	–Grooves
	–Fe, W, Ni, O	–No Co	–Fe, W, Ni, O	
	–No Co		–Fe, W, Ni, C	
FNW/Alumina Ball	–Fe, W, Ni, C, O	No zone	–Fe, W, Ni, C, O	–Grooves
	–Fe, W, Ni, O		–Fe, W, Ni, O	–Largest-flake type debris (5 N; 10 cm s^{-1})
			–Fe, W, C	

of debris and pit formation from eutectic areas is presented in the insert image of figure 7(b). It can be seen: the gray regions are carbides; the lighter areas are iron matrix and the dark spots are voids.

With increase sliding speed (tests conducted at [10 N; 10 cm s^{-1}]), in addition to scratched marks, the wear track of composite disc exhibited the presence of appreciable amount of largest-flake type debris, localized in specific regions (figures 7(c)–(d)) suggesting delamination of the tribo-layer. Thus, similar wear mechanism may be assumed, that is:

i. The local surface temperature and the oxidization rate of the surface layer increased (tribo-layer formation). Some specific regions are more compressed, deformed and oxidized than others because of the heterogeneous microstructure and phase composition of the FNW composite material. Due to the localized high temperature and high pressure during sliding, the tribo-layer becomes subsequently inhomogeneous.

ii. Stress concentration at the layer–core interface at specific regions increases and we observe the appearance of cracks.

iii. It is anticipated that under more intensive and cyclical loading conditions, the cracks coalesced and propagated up to the surface. Consequently, failure of the tribo-layer will occur, leading to the delamination of these specific regions.

Therefore, against alumina balls, increasing the applied load during sliding, has led to the increase of subsurface cracks, of the width and depth of the worn tracks. As the shear stresses applied to subsurface layers of the material during sliding depend directly on the normal force and friction coefficient, increasing the normal load results in increasing shear stresses and leads to the decrease in the facility of cracks propagation. Increasing sliding speed leads to fast increasing in temperature within contact zone and the synergic effect (10 N and 10 cm s^{-1}) was a delamination of the tribo layer in the form of very large flakes or plate-like debris.
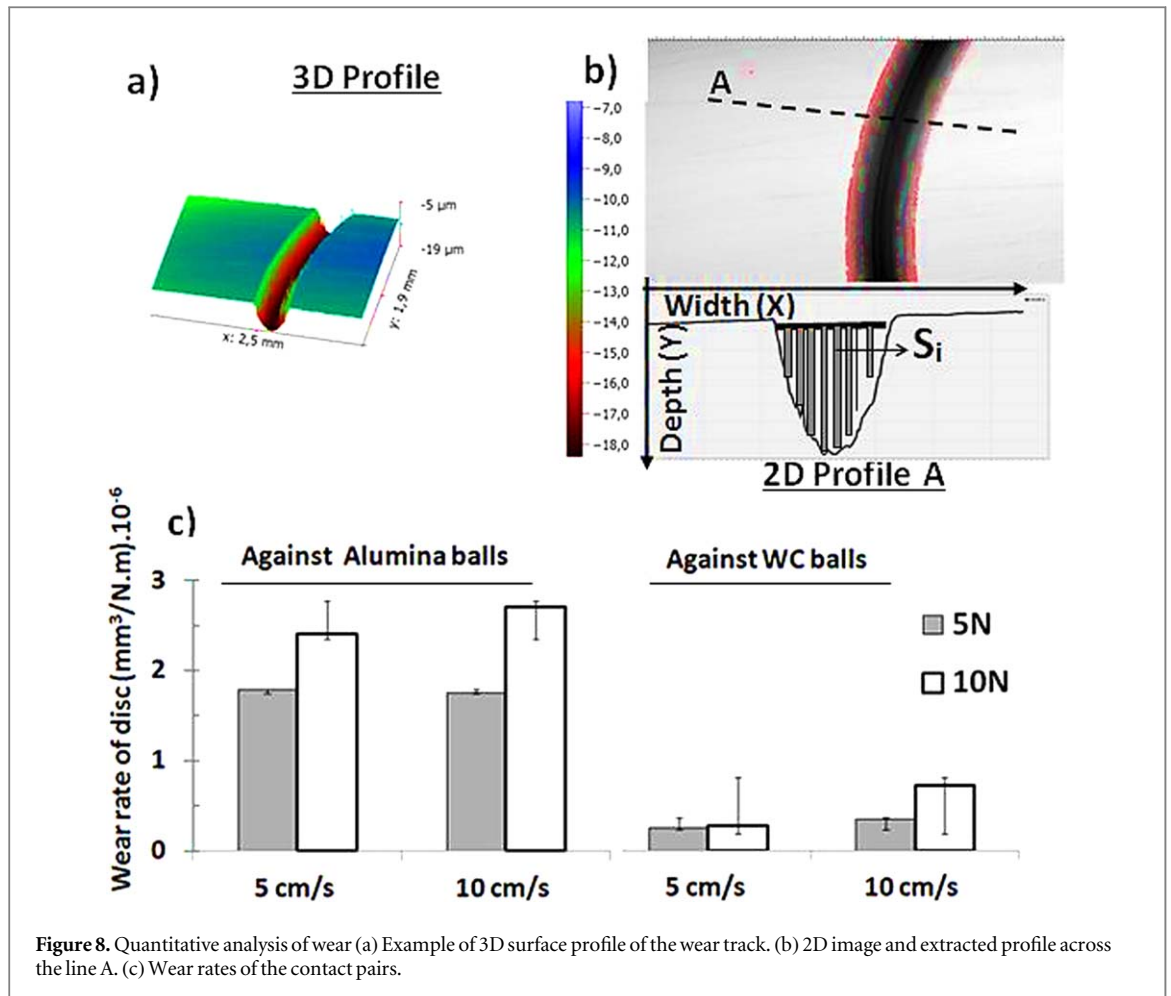
Table 3, summarizes the SEM/EDS analysis results in overall, taken from different areas inside the wear tracks. From table 3, it can be seen that, regardless of test conditions i.e. applied load and sliding speed, EDS confirmed that, in the FNW/WC tribo-pair, the presence of oxygen on the worn surface is indicative of oxidative wear. Grooves, on SEM micrographs are signs of an abrasive wear and absence of Co signal implies that, there is no material transfer from the WC ball. Isolated particles (Wear debris) are mainly constituted of oxides and carbides. The FNW/Al$_2$O$_3$ tribo-pair shows signs of oxidative and abrasive wear as in WC ball case. Besides a delamination wear occurs at [10 N; 10 cm s^{-1}] conditions.

3.4. Wear rates
Wear rates (K) are calculated via volume loss of the wear tracks at different locations. At each location, for example location 'A' in figures 8(a)–(b), an XY profile (2D profile: width/depth) was extracted and the surface S was calculated following equation (2):

$$S = \sum S_i = \sum_{i=0}^{n} [(x_{i+1} - x_i).(y_i)] \tag{2}$$

The equation (2) gives a best approximation of the cross-sectional surface estimation -S (S = Σ S$_i$; S$_i$ -is the surface of the little rectangles (Δx; Δy)). The volume loss was automatically calculated by the software of the optical profilometry, as the transversal section –S multiplying by the circumference $2\pi r$ (r is the track radius). Errors ($\Delta V/V$) were estimated based on six (06) locations per wear track at least.

Figure 8. Quantitative analysis of wear (a) Example of 3D surface profile of the wear track. (b) 2D image and extracted profile across the line A. (c) Wear rates of the contact pairs.

In this work, quantification of the wear volume loss of balls was difficult and not reproducible. Then, the obtained values of wear rate of alumina balls were not reliable. Thus, that is why wear rates of balls are not taking into account.

Numerical values of roughness and wear rates (K) obtained for different contact pairs after wear tests are presented in figure 8. It is obvious that the wear rates of the tested samples are remarkably different. The minimum wear rate was found in the FNW/WC contact pair at [5 N; 5 cm s^{-1}]. The maximum wear rate was obtained in the FWN/Alumina contact pair at [10 N; 10 cm s^{-1}]. The wear rate $K_{Alumina}$ is ten times higher than K_{WC}. So Alumina balls cause more damage than WC on sample surfaces.

Against WC balls, the ratio K_{10N}/K_{5N} at [5 cm s^{-1} and 10 cm s^{-1}] was ~1.1 and ~2 respectively. Samples loaded under 5 N exhibit approximately similar wear rates at [5 and 10 cm s^{-1}]. However, when loaded at 10 N, the wear rate at 10 cm s^{-1} is twice than the one at 5 cm s^{-1}.

Against Alumina balls the ratio K_{10N}/K_{5N} evolves from 1.3 ± 0.02 at 5 cm s^{-1} to ~1.5 ± 0.02 at 10 cm s^{-1}. Consequently, increasing the load leads to the wear rate increase regardless of the sliding speed and whatever the counterpart (WC or Alumina ball) as expected.

The difference in wear track morphologies and wear rates of the FNW samples sliding against two different counterpart materials cannot be attributed only to the difference in hardness as demonstrated in a previous study [37].

The wear product plays a key role in such situation [38]. Indeed, Li *et al* explain that WC debris (particles from WC ball) produced less wear loss than Alumina debris because of their small quantities and their shape [39]: Al_2O_3 particles are sharp and angular, so more abrasive. In addition to abrasive wear, samples tested at [10 N and 10 cm s^{-1}], undergo a delamination wear leading to more excessive wear loss as demonstrated by SEM analysis in figures 7(c)–(d). So, the difference between the wear of these two contact systems (FNW/WC and FNW/Alumina) also resulted from their different wear debris removal mechanisms.

4. Conclusion

In this paper, WC particle–reinforced iron matrix composites were elaborated using powder metallurgy route process. The most important conclusions we have reached through this study are:

1. The microstructure of the composite consists of a dendrites matrix of γ- austenite, primary and secondary carbides and eutectic.

2. Normal load and sliding speed affect the friction force and wear rate considerably. Formation of tribo-layers and wear debris are also main factors.

3. At the steady state, the average value of the COF depends on the applied load regardless of sliding speed.

4. Oxidative and abrasive wear are the main wear mechanisms observed in this study. However, a delamination wear as third process, occurs in the special case of 10 N and 10 cm s^{-1} against alumina.

5. Wear rates of the FNW/Al$_2$O$_3$ couple are higher than the FNW/WC couple ones. The highest COF are found for the FNW/Alumina ball contact pairs.

Acknowledgments

ORCID iDs

A Grairia ⓘ https://orcid.org/0000-0002-1006-074X

References

[1] Silvestroni L, Pienti L, Guicciardi S and Sciti D 2015 Strength and toughness, the challenging case of TaC-based composites *Composites Part B: Engineering* **72** 10–20
[2] Huth S, Krasokha N and Theisen W 2009 Development of wear and corrosion resistant cold-work tool steels produced by diffusion alloying *Wear* **267** 449–57
[3] Razavi M, Yaghmaee M S, Rahimipour M R and Tousi S R 2010 The effect of production method on properties of Fe–TiC composite *Int. J. Miner. Process.* **94** 97–100
[4] Jiang Q C, Zhao F, Wang H Y and Zhang Z Q 2005 *In situ* TiC-reinforced steel composite fabricated via self-propagating high-temperature synthesis of Ni–Ti–C system *Mater. Lett.* **59** 2043–7
[5] Li B, Liu Y, Cao H, He L and Li J 2009 Rapid fabrication of *in situ* TiC particulates reinforced Fe-based composites by spark plasma sintering *Mater. Lett.* **63** 2010–2
[6] Song B, Dong S, Coddet P, Zhou G, Ouyang S and Liao H 2013 Microstructure and tensile behavior of hybrid nano-micro SiC reinforced iron matrix composites produced by selective laser melting *J Alloy Compd* **579** 415–21
[7] Nair F, Cerit A A and Karamis M B , 2015 Wear behaviour of aluminum matrix sic particle reinforced composite cam profile under dry sliding condition *J Balk Tribol Assoc* **21** 186–94
[8] Zhong L, Xu Y, Li C, Ye F, Liu X and Hojamberdiev M 2012 Infiltration casting and *in situ* fabrication of tantalum carbide particulate-reinforced iron matrix composites *J. Compos. Mater.* **46** 895–901
[9] Dammak M, Gaspérini M and Barbier D 2014 Microstructural evolution of iron based metal–matrix composites Unpublished to simple shear *Materials Science and Engineering:* A **616** 123
[10] Zhang Y, Yang B, Han Y, Jiang C, Wu D, Fan J and Ma L 2016 Novel iron metal matrix composite einforced by quartz sand for the effective' *Chemosphere* **146** 308–14
[11] Tang S L, Gao Y M and Li Y F 2014 Critical assessment- Recent developments in fabrication of ceramic particle reinforced iron matrix wear resistant surface composite using infiltration casting technology *Ironmaking Steelmaking* **41** 633–40
[12] Wang X, Zhong L S, Zhao N N, Ovcharenko V E and Xu Y H 2016 A general process for *in situ* formation of iron-matrix composites reinforced by carbide ceramic *Mater. Sci. Forum* **852** 461–6
[13] Zhong L, Hojamberdiev M, Ye F, Wu H and Xu Y 2013 Fabrication and microstructure of *in situ* vanadium carbide ceramic particulates-reinforced iron matrix composites *Ceram. Int.* **39** 731–6
[14] Dyachkova L N and Feldshtein E E 2015 Microstructures, strength characteristics and wear behavior of the Fe-based P/M composites after sintering or infiltration with Cu–Sn alloy *J. Mater. Sci. Technol.* **31** 1226–31
[15] Schubert W D, Fugger M, Wittmann B and Useldinger R 2015 Aspects of sintering of cemented carbides with Fe-based binders *Int. J. Refract. Met. Hard Mater.* **49** 110–23
[16] Cen Q, Jiang Y, Zhou R, Xu Y and Wang J 2011 Study on *in situ* synthesis of TiC particle reinforced iron matrix composite *J. Mater. Eng. Perform.* **20** 1447–50
[17] Wang J and Fu S 2014 Production of *in situ* vanadium carbide particulate reinforced iron matrix composite *Mater Sci Medzg* **20** 409–13
[18] Zhong L, Ye F, Xu Y and Li J 2014 Microstructure and abrasive wear characteristics of *in situ* vanadium carbide particulate-reinforced iron matrix composites *Mater Des (1980-2015)* **54** 564–9

[19] Cao X, Jin J, Zhang Y and Yaping Zong B 2015 Mechanical properties of iron matrix composites reinforced by copper-coated hybrid ceramic particles *J. Mater. Res.* **30** 2360–8

[20] Zhou R, Jiang Y and Lu D 2003 The effect of volume fraction of WC particles on erosion resistance of WC reinforced iron matrix surface composites *Wear* **255** 134–8

[21] Alvarez A E, Oliver C G, Soldera F and García L J 2015 Densification and FIB, SEM, TEM microstructures of WC composites with Fe or Co matrices *Proceedia Mater Sci* **8** 406–13

[22] Wang J, Li L and Tao W 2016 Crack initiation and propagation behavior of WC particles reinforce Fe-based metal matrix composite produced by laser melting deposition *Opt. Laser Technol.* **82** 170–82

[23] Li Z, Jiang Y, Zhou R, Gao F, Shan Q and Tan J 2014 Thermal fatigue mechanism of WC particles reinforced steel substrate surface composite at different thermal shock temperatures *J Alloy Compd* **596** 48–54

[24] Madej M 2013 Phase reactions during sintering of M3/2 based composites with WC additions *Arch Metall Mater* **58** 703–8

[25] Li Z, Jiang Y, Zhou R, Chen Z, Shan Q and Tan J 2014 Effect of Cr addition on the microstructure and abrasive wear resistance of WC-reinforced iron matrix surface composites *J. Mater. Res.* **29** 778–85

[26] Sinha A and Farhat Z 2015 A study of porosity effect on tribological behavior of cast Al A380M and sintered Al 6061 alloys *J Surf Eng Mater Adv Technol* **5** 1

[27] Chen Q, Li D Y and Cook B 2009 Is porosity always detrimental to the wear resistance of materials?—A computational study on the effect of porosity on erosive wear of TiC/Cu composites *Wear* **267** 1153–9

[28] Fernandes C M and Senos A M R 2011 Cemented carbide phase diagrams: a review *Int. J. Refract. Met. Hard Mater.* **29** 405–18

[29] Gong X, Fan J L, Ding F, Song M and Huang B Y 2012 Effect of tungsten content on microstructure and quasi-static tensile fracture characteristics of rapidly hot-extruded W–Ni–Fe alloys *Int. J. Refract. Met. Hard Mater.* **30** 71–7

[30] Bhushan B 2013 *Principles and Applications of Tribology* (Chichester: Wiley)

[31] Gras R 2008 *Tribologie principes et solutions industrielles* (Paris: Dunod) pp 131–73

[32] Hisakado T, Miyazaki K, Kameta A and Negishi S 2000 Effects of surface roughness of roll metal pins on their friction and wear characteristics *Wear* **239** 69–76

[33] Findik F 2014 Latest progress on tribological properties of industrial materials *Mater. Des.* **57** 218–44

[34] Pirso J, Letunovitš S and Viljus M 2004 Friction and wear behaviour of cemented carbides *Wear* **257** 257–65

[35] Niu Q, Zheng X, Chen M and Weiwei M 2014 Study on the tribological properties of titanium alloys sliding against WC–Co during the dry friction *Ind Lubr Tribol* **66** 202–8

[36] Prabu S S, Prathiba S, Asokan M A, Jain A, Jain N K and Chourasiya P K 2014 Investigations on dry sliding wear behaviour of sintered/extruded P/M alloy steels (Fe–C–W–Ti) *Procedia Eng* **97** 2119–26

[37] Beliardouh N E, Nouveau C and Kaleli H 2014 Wear performance of duplex treated low alloyed steel against wood (beech) as static partner *J. Balk. Tribol. Assoc.* **20** 84–92

[38] Zivic F, Babic M, Grujovic N, Mitrovic S, Adamovic D and Favaro G 2012 A comparison of reciprocating sliding at low loads and scratch testing for evaluation of TiN(PVD) coating *J Balk Tribol Assoc* **18** 80–91

[39] Li C X, Xia J and Dong H 2006 Sliding wear of TiAl intermetallics against steel and ceramics of Al_2O_3, Si_3N_4 and WC/Co *Wear* **261** 693–701